ARTICLES
https://doi.org/10.1038/s41563-020-0756-y

nature materials

Check for updates

Extra storage capacity in transition metal oxide lithium-ion batteries revealed by in situ magnetometry

Qiang Li[1,2,7]✉, Hongsen Li[1,3,7]✉, Qingtao Xia[1,7], Zhengqiang Hu[1,7], Yue Zhu[3], Shishen Yan[4], Chen Ge[5], Qinghua Zhang[5], Xiaoxiong Wang[1], Xiantao Shang[1], Shuting Fan[1], Yunze Long[1], Lin Gu[5], Guo-Xing Miao[1,2,6]✉, Guihua Yu[3]✉ and Jagadeesh S. Moodera[6]

In lithium-ion batteries (LIBs), many promising electrodes that are based on transition metal oxides exhibit anomalously high storage capacities beyond their theoretical values. Although this phenomenon has been widely reported, the underlying physicochemical mechanism in such materials remains elusive and is still a matter of debate. In this work, we use in situ magnetometry to demonstrate the existence of strong surface capacitance on metal nanoparticles, and to show that a large number of spin-polarized electrons can be stored in the already-reduced metallic nanoparticles (that are formed during discharge at low potentials in transition metal oxide LIBs), which is consistent with a space charge mechanism. Through quantification of the surface capacitance by the variation in magnetism, we further show that this charge capacity of the surface is the dominant source of the extra capacity in the Fe_3O_4/Li model system, and that it also exists in CoO, NiO, FeF_2 and Fe_2N systems. The space charge mechanism revealed by in situ magnetometry can therefore be generalized to a broad range of transition metal compounds for which a large electron density of states is accessible, and provides pivotal guidance for creating advanced energy storage systems.

Since the first rechargeable lithium-ion battery (LIB) was developed, such batteries have received a great deal of attention as they enable the development of increasingly capable and versatile electronic devices[1–3]. To further improve the energy storage capacity of LIBs, considerable research efforts have been devoted to electrode materials that are based on transition metal oxides and that feature a conversion-type reaction mechanism. The capacities of such materials can reach extraordinarily high values (700–1,200 mAh g^{-1}) that are about three times higher than that of commercialized graphitic carbon[4,5]. Although these materials inevitably suffer from a large hysteresis between the discharge and charge steps, which causes difficulties in practical applications[6], an intriguing finding with these transition metal oxides is that they have extra capacities beyond the theoretical limit, the underlying mechanisms for which have been the subject of intense debates[7]. In 2002, a possible correlation was suggested[8] between the extra electrochemical capacity for metal-oxide/Li cells and the growth of a polymer or gel-like film around the metallic (M^0) nanograins in a window of low discharge voltage; this extra capacity could be maintained over hundreds of cycles. Later, an interfacial storage theory[9–12] proposed that the excess Li^+ ions can be accommodated at the M^0–Li_2O interfaces while electrons are confined on the metallic side. Recently, an ex situ solid-state NMR technique was used[7] to track the evolution of ^6Li, ^{17}O and ^1H signals at different discharge depths in the RuO_2/Li battery system, which showed that the additional capacity probably lies in the reversible surface conversion of LiOH to Li_2O and LiH. Although several plausible theories have been proposed, no agreement has been reached until now owing to the complexity of the electrochemical processes and the difficulty of probing the intrinsic property change that occurs at the metal–salt interfaces, which is beyond the capabilities of many conventional characterization tools.

The magnetism of electrodes that are based on transition metals and their compounds is sensitive to the transfer of electrons (whether on the surface of the material or in the bulk) during the charge storage process[13–18]. For this reason, we used in situ magnetometry to investigate the evolution of the internal electronic structure in a typical Fe_3O_4/Li cell in real time. Most surprisingly, the reduced metallic Fe^0 in the Fe_3O_4/Li cell can continue to participate in the lithium storage reaction during the discharging process at low voltage, which is associated with a notable decrease in magnetization in the electrodes. Specifically, a strong surface capacitance of Fe nanoparticles was detected during the in situ magnetometry of the Fe/Li_2O systems. We propose that during the discharge at low potentials in the Fe^0/Li_2O nanocomposites, spin-polarized electrons are injected into Fe nanoparticles to a depth on the order of the Thomas–Fermi screening length and form a space charge zone[19], while excess Li^+ ions are stored at the grain boundaries and surfaces. Moreover, in situ magnetometry quantitatively reveals that the charge capacity of the surface is the dominant source of the extra capacity in the Fe_3O_4/Li system. In addition, we show that the

[1]College of Physics, Center for Marine Observation and Communications, Qingdao University, Qingdao, China. [2]Department of Electrical and Computer Engineering and Institute for Quantum Computing, University of Waterloo, Waterloo, Ontario, Canada. [3]Materials Science and Engineering Program and Department of Mechanical Engineering, The University of Texas at Austin, Austin, TX, USA. [4]School of Physics, State Key Laboratory of Crystal Materials, Shandong University, Jinan, China. [5]Beijing National Laboratory for Condensed Matter Physics, Institute of Physics, Chinese Academy of Sciences, Beijing, China. [6]Department of Physics, Plasma Science and Fusion Center and Francis Bitter Magnet Laboratory, Massachusetts Institute of Technology, Cambridge, MA, USA. [7]These authors contributed equally: Qiang Li, Hongsen Li, Qingtao Xia, Zhengqiang Hu. ✉e-mail: liqiang@qdu.edu.cn; hsli@qdu.edu.cn; guo-xing.miao@uwaterloo.ca; ghyu@austin.utexas.edu

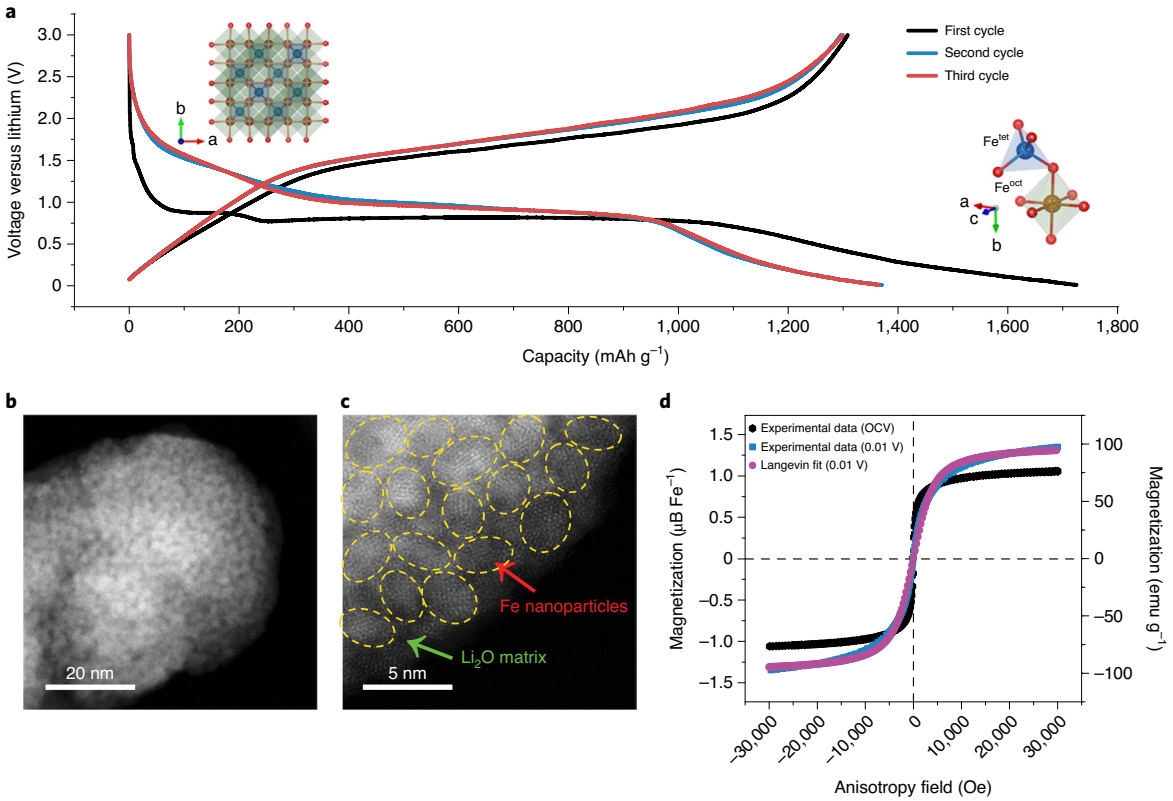

Fig. 1 | Characterization of the Fe_3O_4 electrode. a, Galvanostatic charge–discharge curves of an Fe_3O_4/Li cell cycled at a current density of 100 mA g^{-1}. The insets show the inverse spinel structure of the crystals. Voltage versus lithium refers to the voltage relative to a reference lithium metal electrode. Oct, octahedral; tet, tetrahedral. **b**, BF-STEM image of the fully lithiated Fe_3O_4 electrode. **c**, High-resolution BF-STEM image showing the presence of Li_2O and Fe inside the agglomerate. **d**, Magnetic hysteresis curves of the Fe_3O_4 electrode before (black) and after (blue) the lithiation process, and the Langevin fitting curve for the latter (violet). We disassembled the battery at 0.01 V and measured the magnetic hysteresis ex situ.

same spin-polarized surface capacitance exists in CoO, NiO, FeF_2 and Fe_2N electrodes, all of which can generate ferromagnetic or superparamagnetic particles during lithiation and exhibit a similar magnetization evolution. This indicates that the surface capacitance of metal nanoparticles can be generalized to a broad range of transition metal compounds in which a large electron density of states is accessible. Here, we reveal the role of the electron density of states in inducing extra energy storage well beyond electrochemistry-driven conversion reactions, which represents a step forward for future high-density energy storage devices that are based on transition metal electrodes.

Structural characterization and electrochemical properties

We synthesized monodispersed hollow Fe_3O_4 nanospheres by using a traditional hydrothermal method, and characterized the morphology and structure of these nanospheres (Supplementary Fig. 1). The electrochemical activity of Fe_3O_4 in LIBs was evaluated in a CR2032 coin-type battery geometry with lithium metal as the counter-electrode. Electrochemical discharge–charge profiles of an Fe_3O_4/Li battery operated at a current density of 100 mA g^{-1} were obtained (Fig. 1a). The first discharge capacity was recorded to be 1,718 mAh g^{-1}, and it stabilized to 1,370 mAh g^{-1} and 1,364 mAh g^{-1} for the second and third cycles, respectively, which well exceeds the theoretical expectation of 926 mAh g^{-1}. High-resolution bright-field scanning transmission electron microscopy (BF-STEM) images of the fully discharged products (Fig. 1b,c) indicate that after reduction by lithium, the Fe_3O_4 nanospheres were converted into smaller Fe nanoparticles with dimensions around 1–3 nm that were dispersed inside a Li_2O matrix, which is consistent with the well-accepted reaction pathway for transition metal oxide electrodes (equation (1))[20].

$$T_x^M O_y + 2ye^- + 2yLi^+ \rightleftarrows x\left[T^M\right]^0 + yLi_2O, \quad (1)$$

where T^M represents a transition metal.

Ex situ X-ray photoelectron spectroscopy (XPS) characterizations also demonstrated that the transition metal oxides were mostly transformed to metals after discharge (Supplementary Fig. 2). To prove the change in magnetic properties during electrochemical cycling, we obtained the magnetization curve after full discharge to 0.01 V (Fig. 1d, with the before-discharge, ferromagnetic Fe_3O_4 curve shown for comparison), which displays superparamagnetic behaviour owing to the formation of nanosized Fe particles. This curve could be fitted by the Langevin equation with an average particle size of around 2.8 nm (Supplementary Information, section II), which is in agreement with sizes indicated in the BF-STEM images.

Real-time detection of structural and magnetic evolution

To correlate the electrochemistry with the structural and magnetic changes in Fe_3O_4, we conducted in situ X-ray diffraction (XRD) and in situ magnetometry studies on the Fe_3O_4 electrodes. The background of the XRD pattern (Supplementary Fig. 3, obtained in the absence of Fe_3O_4 active materials) is attributed to the beryllium window from the experimental setup and the lithium metal from the counter-electrode. In the initial discharge from the open-circuit voltage (OCV) to 1.2 V, the Fe_3O_4 diffraction peaks in the series of XRD diffraction patterns exhibited no notable changes in either intensity or position (Fig. 2a), which

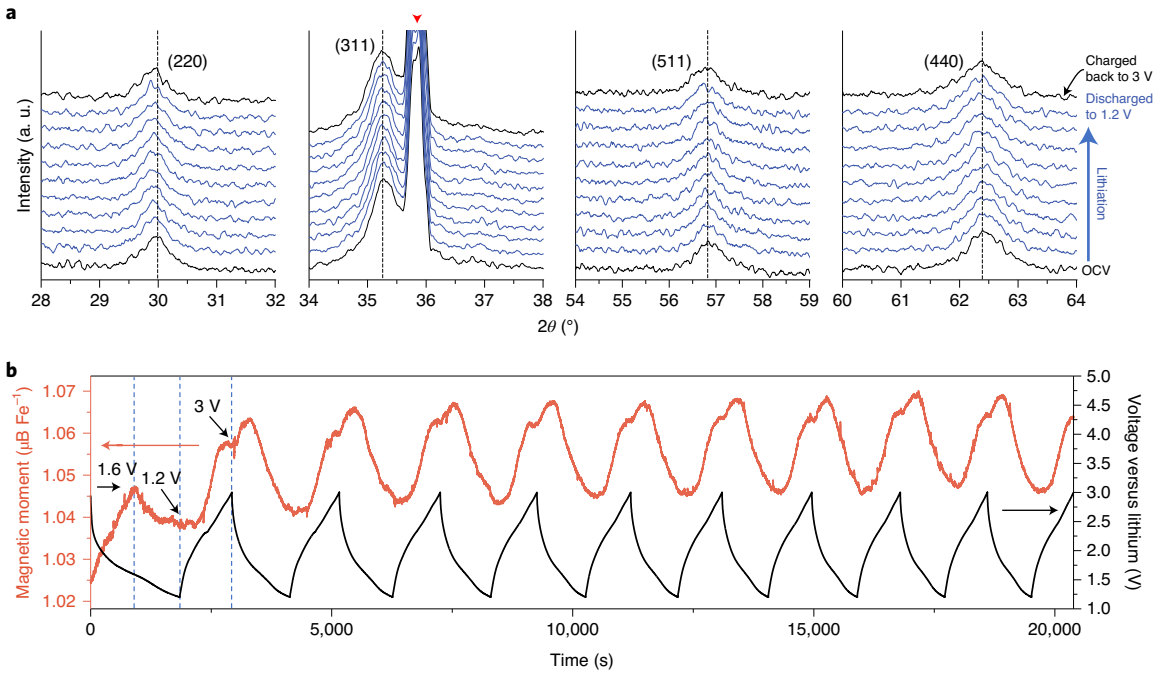

Fig. 2 | In situ XRD and magnetic monitoring characterizations. a, In situ XRD patterns show the evolution of (220), (311), (511) and (440) Bragg reflections of Fe_3O_4 in the potential range from the OCV to 1.2 V at a current density of 60 mA g^{-1}. The peak (middle left panel, marked with a red arrowhead) corresponds to lithium. a.u., arbitrary units. **b**, The electrochemical charge–discharge profiles of Fe_3O_4 and the corresponding reversible in situ magnetic response at an applied magnetic field of 3 T.

indicates that the Fe_3O_4 undergoes a Li intercalation process only. When charged back to 3 V, the inverse spinel structure of the Fe_3O_4 remained well preserved, which demonstrates that the process in this voltage window is highly reversible in nature. We carried out further in situ magnetometry that was combined with galvanostatic charge–discharge tests to study how the magnetization evolves in real time (Fig. 2b). The time-sequenced magnetic responses recorded the saturation magnetization of the Fe_3O_4 electrode during the lithium intercalation process. The saturation magnetization $\mathcal{M}$s rose slightly when the discharge potential decreased from the OCV to 1.6 V. This change in the magnetization that is detected in situ can be attributed to the reduction and displacement of the Fe^{3+} ions. As the Fe^{3+} ions of Fe_3O_4 at the A (tetrahedral) and B (octahedral) sites are aligned in an antiparallel fashion, the net magnetic moment results from only the Fe^{2+} (4 μB) ions at the B sites (see Supplementary Fig. 4a for the Fe_3O_4 spin configurations)[13,17,21–23]. During the initial stage of lithium intercalation, both the reduction of Fe^{3+} (5 μB) to Fe^{2+} (4 μB) at the A sites and their migration to the B sites can increase the net magnetic moment (see corresponding schematic diagram in Supplementary Fig. 4b). Upon further lithiation, $\mathcal{M}$s decreased to 1.038 μB Fe^{-1} at the terminal discharge potential (1.2 V). This is because the reduction of Fe^{3+} ions at the B sites controls the overall magnetic response, which can cause a substantial reduction in the net magnetic moment. The evolution of the magnetic response is consistent with the cyclic voltammetry curves of the Fe_3O_4 electrode (Supplementary Fig. 5). Note that the magnetic variation that accompanies the first discharge process seems only partially reversible, which may be due to the irreversible incorporation of a small number of Li^+ ions in vacancies and/or defects in the Fe_3O_4 (ref. [24]).

With intercalation of Li^+ ions into Fe_3O_4 at the initial stage, the inverse spinel phase slowly goes through lattice reconstruction to an intermediate rock-salt-like phase $Li_xFe_3O_4$ ($0<x<2$)[17,21,22]. Further lithiation triggers the formation of a cation-segregated rock-salt phase (Li_2O·FeO) and finally the conversion into metallic Fe^0 and Li_2O (ref. [23]). The full electrochemical reaction pathway can be given as follows:

$$Fe_3O_4 + 8e^- + 8Li^+ \rightarrow 3Fe^0 + 4Li_2O, \quad (2)$$

$$Fe + Li_2O \rightarrow FeO + 2Li^+ + 2e^-. \quad (3)$$

For a more fundamental understanding of this conversion process in terms of the change in magnetization, we collected the magnetic responses together with the corresponding phase changes that accompany the electrochemically driven reactions down to 0.01 V in real time (Fig. 3). Clearly, the Fe_3O_4 electrode magnetization response in the first discharge is different from those of the other cycles, which is due to the irreversible phase transformation of Fe_3O_4 during the first lithiation. When the potential decreased to 0.78 V, the inverse spinel phase of Fe_3O_4 was transformed to an FeO-like rock-salt structure with Li_2O, and that Fe_3O_4 phase could not be recovered upon charging, as discussed in previous reports[21–23,25,26]. Correspondingly, the magnetization experienced a rapid decrease down to 0.482 μB Fe^{-1}. As the lithiation proceeded, there was no evidence of new phase formation and the intensities of the (200) and (220) FeO-like diffraction peaks began to weaken. No pronounced XRD peaks remained when the Fe_3O_4 electrode was fully lithiated (Fig. 3a). It is reasonable to assume that the reduced products that consisted of small metallic Fe^0 nanograins inside the Li_2O matrix were not identifiable through XRD[25]. We noticed that a pronounced increase in the magnetization (from 0.482 μB Fe^{-1} to 1.266 μB Fe^{-1}) occurred when the Fe_3O_4 electrode was discharged from 0.78 V to 0.45 V, which is attributed to the conversion reaction from FeO to Fe. The magnetization then decreased slowly to a value of 1.132 μB Fe^{-1} at the end of the discharge. This finding suggests that the fully reduced metallic Fe^0 nanograins could still be involved in the lithium storage reaction and thereby reduce the magnetization of the electrodes, which contradicts the

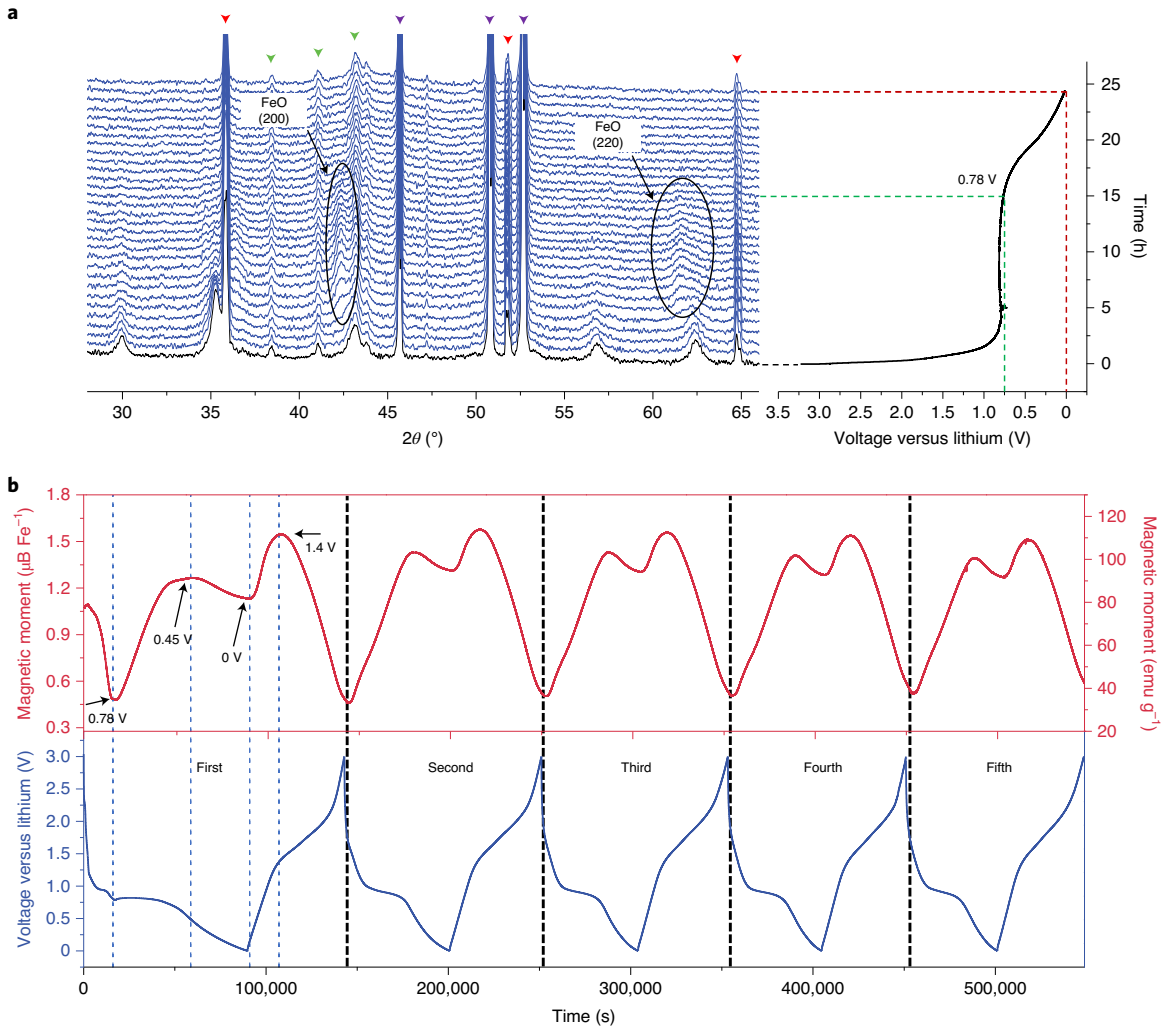

Fig. 3 | In situ observation of the phase transformation and magnetic response. a, In situ XRD patterns collected during the first discharge of an Fe_3O_4 electrode at a current density of 60 mA g^{-1} in the potential window between the OCV and 0.01 V. The peaks marked with red, green and purple arrowheads correspond to Li, BeO and Be, respectively. **b**, In situ magnetometry in an Fe_3O_4/Li cell as a function of electrochemical cycling under an applied magnetic field of 3 T.

classic understanding of conversion mechanisms in LIBs. Some reduction of residual Fe^{2+} to Fe^0 may occur, but the reduction is very unfavourable at low potentials. Interestingly, the subsequent charging up to 1.4 V resulted in a second increase in the magnetization (to 1.546 μB Fe^{-1}). Further delithiation led to a sharp decrease in the magnetic response owing to the oxidation of the metal, as evidenced by supporting ex situ STEM and XPS measurements (Supplementary Fig. 6). Nevertheless, no phase changes or formation of iron oxide were observed in the in situ XRD measurements (Supplementary Figs. 7,8). After the first cycle was completed, the observed magnetic responses were found to be highly reversible (Fig. 3b) and could always be correlated to the electrode potential. Similarly, such potential-dependent magnetization variation was measured in cyclic voltammetry tests at a scan rate of 0.25 mV s^{-1} (Supplementary Fig. 9). Overall, one of the most important findings from the in situ magnetic monitoring is that the metallic Fe^0 reduced from Fe_3O_4 can continue to participate in the electrically driven lithiation reaction, which results in diminished magnetization for the battery electrode.

Surface capacitance revealed by magnetometry in the Fe^0/Li_2O system

The magnetization changes of the Fe_3O_4 electrode occurred at low voltages at which extra electrochemical capacity is most likely to be generated[8], and this suggests the existence of undiscovered charge carrier reservoirs inside the battery. To explore the underlying lithium storage mechanism, we studied Fe_3O_4 electrodes at the magnetization peaks (0.01 V, 0.45 V and 1.4 V) by means of XPS, STEM and magnetic characterizations to identify the origin of the magnetism variation. The XPS results (Supplementary Figs. 2a,10) show no voltage dependence, and no unexpected reactions such as Fe–C bonding are observed (Supplementary Fig. 11). This demonstrates that transition metal oxides have been mostly reduced to metals in this voltage region with no other complicating chemical reactions. Moreover, no noticeable change in Fe particle morphology is observed in the STEM images (Fig. 1c and Supplementary Fig. 12). Furthermore, the magnetic interactions change slightly when evaluated as a function of the blocking temperature in field cooling and zero-field cooling curves[27] (Supplementary Fig. 13). As subtle variations among the particles, such as inhomogeneous particle size and shape, interparticle coupling, and magnetocrystalline anisotropy within particles, can also induce magnetism variation in low magnetic fields, we measured magnetization in high fields that approach saturation magnetization to eliminate these complications (Supplementary Fig. 14). Our results indicate that the magnetic moment is the key factor in the magnetic changes, because the measured $\mathcal{M}$s of the Fe^0/Li_2O system is not influenced by magnetic anisotropy or interparticle coupling.

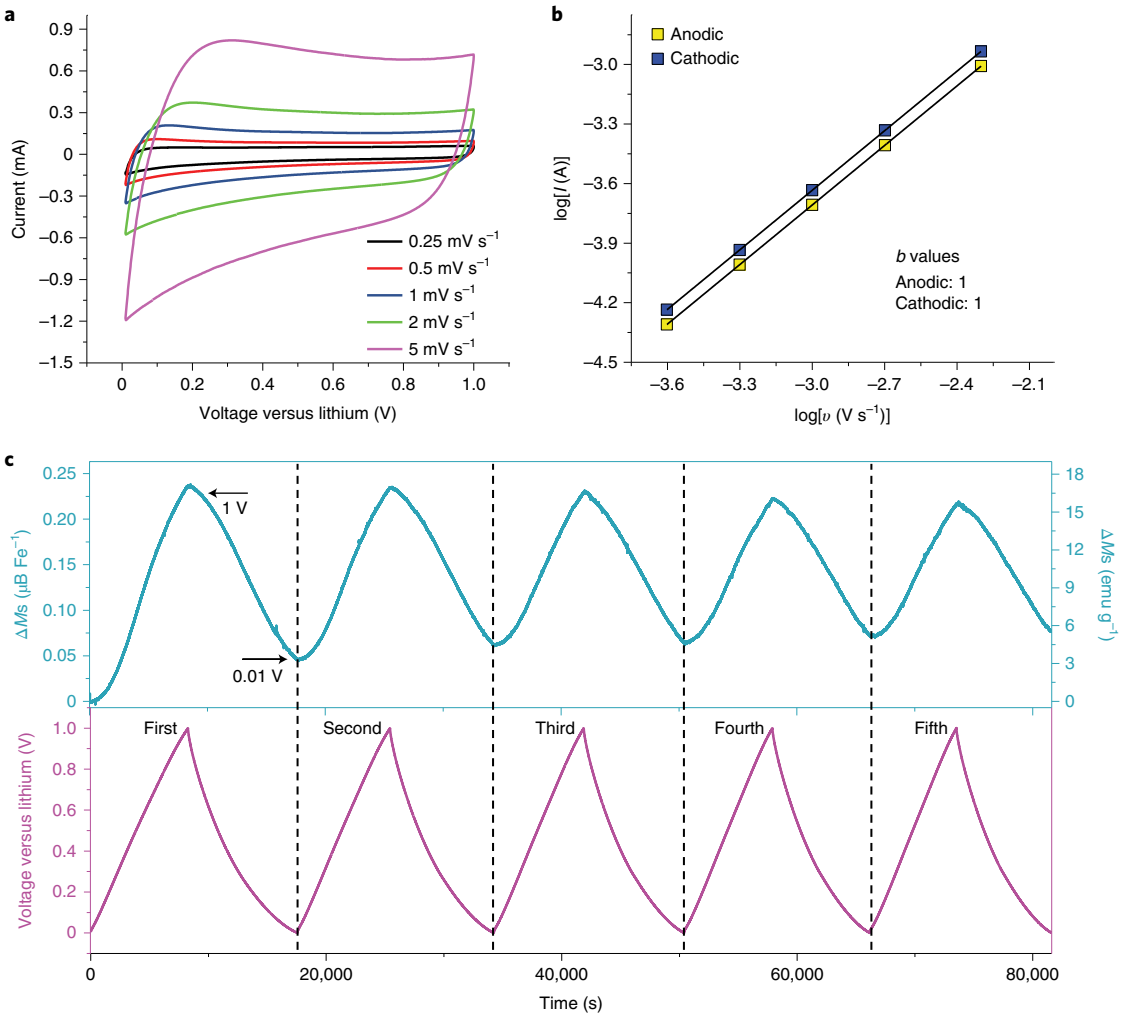

Fig. 4 | Electrochemical performance and in situ magnetic characterization in the potential window of 0.01–1 V. a, Cyclic voltammetry curves of an Fe_3O_4/Li cell that was discharged down to 0.01 V at various rates. **b**, Determination of the *b* value by using the correlation between peak current and sweep rate. **c**, The reversible variation of magnetization at an applied magnetic field of 5 T with respect to the charge–discharge curves.

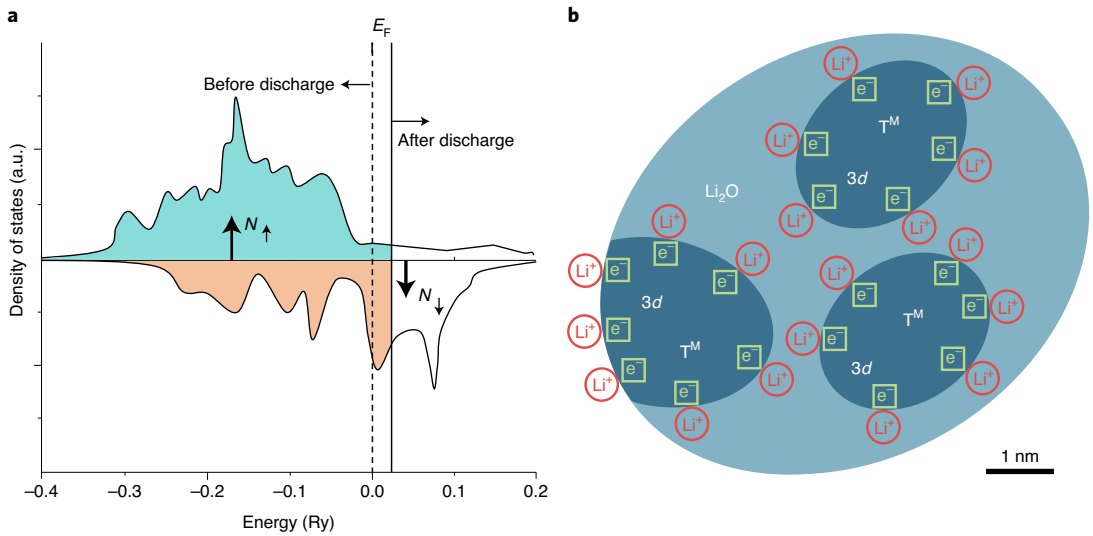

Fig. 5 | Schematic of surface capacitance with spin-polarized electrons at the Fe/Li_2O interface. a, Schematic of spin-polarized density of states at the surface of ferromagnetic metal grains (before and after discharge), which is opposite to the bulk spin polarization for the case of Fe. E_F, Fermi energy. **b**, Formation of a space charge zone in the surface capacitance model for extra lithium storage.

Considering possible side reactions of the electrolyte at low voltage and the complexity of the nanoparticle electrode that is mixed with binders and conductive additives, we prepared $(Fe/TiO_2)_{15}$ layered composites with different nanoscales of Fe particles by layer-by-layer deposition with magnetron sputtering, and assembled thin-film batteries (which are cleaner systems than the traditional ones) in which TiO_2 can provide lithium-ion transmission channels and limit the size of Fe nanoparticles. The cyclic voltammetry curves of the $(Fe(1\,nm)/TiO_2(3\,nm))_{15}$ electrode at high potential exhibit a semi-rectangular shape (Supplementary Fig. 15a), which usually represents capacitive or pseudocapacitive behaviour[8]. More importantly, this electrode exhibits the same magnetization variation as that shown in the low voltage region for the Fe_3O_4/Li cell (Fig. 3b), whereas we can observe hardly any variation of magnetism in the $(Fe(10\,nm)/TiO_2(3\,nm))_{15}$ electrode (Supplementary Fig. 15b). These results imply that the magnetism variation at low voltage for the Fe_3O_4 electrode is associated with a capacitive-type behaviour of the reduced Fe nanoparticles, which is believed to play an important role in the observed extra storage capacity.

To further understand the kinetic properties of the Fe_3O_4 electrode at low voltage, we performed cyclic voltammetry measurements at various scan rates. The cells were discharged down to 0.01 V in advance. Similar to the result of the $(Fe(1\,nm)/TiO_2(3\,nm))_{15}$ electrode, rectangular cyclic voltammetry curves appear in the voltage range between 0.01 V and 1 V (Fig. 4a). To gain further insight, we plotted the variation of log I as a function of log υ, where I is the current and υ is the sweep rate. In general, the current obeys a power-law relationship with the sweep rate in the form of $i = a\upsilon^b$, where a and b are adjustable parameters[28,29]. For sweep rates that range from 0.25 mV s^{-1} to 5 mV s^{-1}, the b values for both the cathodic and anodic peaks were found to be equal to 1 (Fig. 4b), which suggests that a capacitive response occurred on the Fe_3O_4 electrode. A highly reversible magnetic response accompanied the constant-current charge–discharge processes (Fig. 4c). The magnetization of the electrode decreased in the discharging process from 1 V to 0.01 V and increased anew in the charging process, which demonstrates that the capacitive-like surface reaction that involves metallic Fe^0 is highly reversible.

The observed electrochemical, structural and magnetic features of the Fe_3O_4 electrode suggest that it is the spin-polarized surface capacitance of Fe^0 nanoparticles that accounts for the extra lithium storage capacity that accompanies the magnetism variation. The spin-polarized capacitance is a result of the accumulation of spin-polarized charges at the interfaces and can show magnetic responses during the charge–discharge processes[30]. For example, with electrostatic charge accumulation at the surface, coercivity modulations of −4.5% and +1% have been achieved in 2-nm-thick films of FePt and FePt in NaOH electrolyte, respectively[14]. In addition, in Fe/MgO/polyimide/indium tin oxide junction capacitors, the electron filling of 3*d* orbitals in the Fe layer caused a large change of 40% in the magnetic anisotropy[31]. As for the Fe_3O_4-based electrode, fine Fe nanoparticles dispersed in a Li_2O matrix with a large surface-to-bulk ratio[23] and a high density of states at the Fermi level owing to the highly localized *d* orbitals[32] can be created during the first discharge. In accordance with Maier's theoretical model of space charge storage[11,12,19,33,34], we propose that a large number of electrons can be stored in the spin-split bands of the metallic Fe nanoparticles, which may generate the spin-polarized surface capacitance in the Fe/Li_2O nanocomposites (Fig. 5). The accumulation of spin-polarized charges within the first few atomic layers at the metal–insulator interface can produce a notable change in the interface magnetization, which depends on the surface electron density of states of the ferromagnetic metals and surface spin polarization near the Fermi level[30,35]. In 3*d* transition metals, the different filling of spin-up and spin-down *d* bands is responsible for the ferromagnetism. The spin-up *d* bands are filled much more than the spin-down *d* bands (Fig. 5a), and the net magnetization is given by $\mathcal{M} = (N_\uparrow - N_\downarrow)\mu_B$, where $N_\uparrow$ and $N_\downarrow$ are the total number of electrons for each spin and μ_B is the Bohr magneton. During the discharge of T^M/Li_2O nanocomposites at low potentials, electrons accumulate inside T^M nanoparticles within a Thomas–Fermi screening length and form a space charge zone[19], while Li^+ ions are stored at the grain boundaries and on surfaces (Fig. 5b). Owing to the dominant population of spin-minority states near the Fermi level on the surface of 3*d* ferromagnetic metals[35,36], the electrons accumulate more in the spin-minority bands than in the spin-majority bands (Fig. 5a), which suggests that the change in the saturation magnetization should be a monotonic reduction during the discharge. For iron, this trend is opposite to the Slator–Pauling rule that is valid in bulk 3*d* transition metals and alloys, owing to the different spin-split density of states for the surface and the bulk[35–37]. The conversion reaction of the Fe_3O_4 electrode during the first discharge–charge cycle and the corresponding magnetic moment changes undergo various stages (Supplementary Fig. 16).

Quantification of the surface capacitance of metal nanoparticles

In this capacitive-like Fe^0/Li_2O system, a fraction of the stored charges become spin-polarized and can therefore be detected by our magnetometry measurements. The spin-polarized charge storage (Q^s, in mAh g^{-1}) is related to the extra charge storage (Q^{extra}) that is provided by surface capacitance through the effective spin polarization, $\mathcal{P}$ (equation (4)).

$$Q^s = \mathcal{P} \times Q^{extra}. \tag{4}$$

If we ignore the small contribution from orbital angular momentum, each added electron contributes a magnetic moment of +1 or −1 Bohr magneton, depending on which spin band it enters. Therefore, the net change in surface magnetization $\Delta\mathcal{M}$ at high magnetic fields depends on the accumulation of spin-polarized electrons (with elementary charge e) at the Fermi surface as follows:

$$\Delta\mathcal{M} = \frac{3.6 \times Q^s}{e} \times \mu_B = \frac{3.6 \times Q^{extra}}{e} \times \mathcal{P} \times \mu_B. \tag{5}$$

Based on this equation, we can estimate a capacity of 176–213 mAh g^{-1} from the change in magnetization of 16.3 emu g^{-1} (0.226 μB Fe^{-1}) (Supplementary Fig. 17 and Supplementary Information, section III), which is in qualitative agreement with the value of 229 mAh g^{-1} that is measured directly from the galvanostatic discharge–charge profile in the voltage range of 0.01–1 V. In fact, $\mathcal{M}$s increases upon charging to 1.4 V (Fig. 3b), which indicates that the release of electrons from the 3*d* bands of Fe^0 dominates the low-voltage storage kinetics. To calculate the charge capacity of the surface, we cycled the battery over a wider potential range, between 0.01 and 1.4 V, to produce cyclic voltammetry curves for an Fe_3O_4/Li cell at various sweep rates (Supplementary Fig. 18a). The b values of the cathodic and anodic peaks were 0.99 and 0.94, respectively, which again indicate the kinetics of typical surface-controlled electrochemical processes (Supplementary Fig. 18b). In the magnetic response that accompanied the electrochemical cyclic voltammetry scanning in this defined potential window (Supplementary Fig. 19), a reversible change during the cathodic and anodic scans was found (Supplementary Fig. 19b) that is analogous to the behaviour of the magnetic response in Fig. 4c. These results demonstrate that charge storage in the Fe_3O_4/Li system in the defined potential window is mainly surface-controlled. That is, in the voltage range between 0.01 V and 1.4 V, the cell behaves in a capacitive manner and the space charge storage mechanism plays a dominant role. In addition, we performed a chronopotentiometry test for an Fe_3O_4/Li cell at a current density of 100 mA g^{-1} (Supplementary Fig. 18c). The spe-

cific capacity was as high as 393 mAh g^{-1}, which is very close to the extra capacity (approximately 440 mAh g^{-1}) beyond the theoretical limit, as indicated in Fig. 1a. We determined an order-of-magnitude estimate of the surface capacity of the Fe nanoparticles (assuming that each Fe atom in the first layer absorbs one electron, and that a typical Fe particle of 2 nm corresponds to 10 Fe atom diameters) (Supplementary Information, section IV). The rough geometric estimate of 208 mAh g^{-1} is close to the order of magnitude of our experimental finding. Based on in situ magnetic monitoring, these findings confirm that the space charge storage in the high-density *d* orbitals is the dominant source of extra capacity in Fe_3O_4 electrodes, and therefore opens the possibility of high-density energy storage systems.

We also demonstrated that the extra surface capacitance of metal nanoparticles exists in CoO, NiO, FeF_2 and Fe_2N LIBs (Supplementary Figs. 20–23, with detailed information in Supplementary Information, section V). These results confirm the universally important roles of high-electron-density orbitals such as the *d* orbitals in the transition metal compound-based anode material.

In conclusion, with advanced in situ magnetic monitoring, we investigated the evolution of the internal electronic structure in TM/Li_2O nanocomposites to reveal the origin of extra storage capacity in this type of LIB. The in situ magnetometry clearly demonstrated that in the Fe_3O_4/Li model battery systems during low-voltage discharge, the electrochemically reduced Fe nanoparticles can store a large number of spin-polarized electrons, which results in a large excess capacity and a pronounced change in the interface magnetization. We further quantified the surface capacitance of metal nanoparticles through the variation in magnetization, and found this capacitance to be in close agreement with the experimentally determined capacitance. We also verified the existence of such capacitance in CoO, NiO, FeF_2 and Fe_2N electrode materials. These findings demonstrate the presence of spin-polarized surface capacitance of metal nanoparticles in LIBs, and lay the foundation for the application of such a space charge storage mechanism to a broad range of transition metal compound-based electrode materials. In addition, we have shown that the in situ real-time magnetic monitoring method is a versatile tool to study the evolution of materials related to transition metals in otherwise inaccessible device configurations.

Online content

Any methods, additional references, Nature Research reporting summaries, source data, extended data, supplementary information, acknowledgements, peer review information; details of author contributions and competing interests; and statements of data and code availability are available at https://doi.org/10.1038/s41563-020-0756-y.

Received: 30 April 2019; Accepted: 2 July 2020;
Published online: 17 August 2020

References

1. Poizot, P., Laruelle, S., Grugeon, S., Dupont, L. & Tarascon, J.-M. Nano-sized transition-metal oxides as negative-electrode materials for lithium-ion batteries. *Nature* **407**, 496–499 (2000).
2. Taberna, P. L., Mitra, S., Poizot, P., Simon, P. & Tarascon, J.-M. High rate capabilities Fe_3O_4-based Cu nano-architectured electrodes for lithium-ion battery applications. *Nat. Mater.* **5**, 567–573 (2006).
3. Wu, H. et al. Stable cycling of double-walled silicon nanotube battery anodes through solid–electrolyte interphase control. *Nat. Nanotechnol.* **7**, 310–315 (2012).
4. Palacin, M. R. Recent advances in rechargeable battery materials: a chemist's perspective. *Chem. Soc. Rev.* **38**, 2565–2575 (2009).
5. Cabana, J., Monconduit, L., Larcher, D. & Palacin, M. R. Beyond intercalation-based Li-ion batteries: the state of the art and challenges of electrode materials reacting through conversion reactions. *Adv. Mater.* **22**, E170–E192 (2010).
6. Li, L. et al. Origins of large voltage hysteresis in high-energy-density metal fluoride lithium-ion battery conversion electrodes. *J. Am. Chem. Soc.* **138**, 2838–2848 (2016).
7. Hu, Y.-Y. et al. Origin of additional capacities in metal oxide lithium-ion battery electrodes. *Nat. Mater.* **12**, 1130–1136 (2013).
8. Laruelle, S. et al. On the origin of the extra electrochemical capacity displayed by MO/Li cells at low potential. *J. Electrochem. Soc.* **149**, A627–A634 (2002).
9. Jamnik, J. & Maier, J. Nanocrystallinity effects in lithium battery materials. Aspects of nano-ionics. Part IV. *Phys. Chem. Chem. Phys.* **5**, 5215–5220 (2003).
10. Maier, J. Mass storage in space charge regions of nano-sized systems (Nano-ionics. Part V). *Faraday Discuss.* **134**, 51–66 (2007).
11. Zhukovskii, Y. F., Balaya, P., Kotomin, E. A. & Maier, J. Evidence for interfacial-storage anomaly in nanocomposites for lithium batteries from first-principles simulations. *Phys. Rev. Lett.* **96**, 058302 (2006).
12. Fu, L., Chen, C.-C. & Maier, J. Interfacial mass storage in nanocomposites. *Solid State Ion.* **318**, 54–59 (2018).
13. Dasgupta, S. et al. Intercalation-driven reversible control of magnetism in bulk ferromagnets. *Adv. Mater.* **26**, 4639–4644 (2014).
14. Weisheit, M. et al. Electric field-induced modification of magnetism in thin-film ferromagnets. *Science* **315**, 349–351 (2007).
15. Gershinsky, G., Bar, E., Monconduit, L. & Zitoun, D. Operando electron magnetic measurements of Li-ion batteries. *Energy Environ. Sci.* **7**, 2012–2016 (2014).
16. Yamada, T. et al. In situ seamless magnetic measurements for solid-state electrochemical processes in Prussian blue analogues. *Angew. Chem. Int. Ed.* **52**, 6238–6241 (2013).
17. Yamada, T., Morita, K., Kume, K., Yoshikawa, H. & Awaga, K. The solid-state electrochemical reduction process of magnetite in Li batteries: in situ magnetic measurements toward electrochemical magnets. *J. Mater. Chem. C* **2**, 5183–5188 (2014).
18. Boyanov, S., Womes, M., Monconduit, L. & Zitoun, D. Mössbauer spectroscopy and magnetic measurements as complementary techniques for the phase analysis of FeP electrodes cycling in Li-ion batteries. *Chem. Mater.* **21**, 3684–3692 (2009).
19. Chen, C.-C. & Maier, J. Decoupling electron and ion storage and the path from interfacial storage to artificial electrodes. *Nat. Energy* **3**, 102–108 (2018).
20. Armand, M. & Tarascon, J.-M. Building better batteries. *Nature* **451**, 652–657 (2008).
21. Thackeray, M. M., David, W. I. F. & Goodenough, J. B. Structural characterization of the lithiated iron oxides $Li_xFe_3O_4$ and $Li_xFe_2O_3$ (0<x<2). *Mater. Res. Bull.* **17**, 785–793 (1982).
22. Fontcuberta, J., Rodríguez, J., Pernet, M., Longworth, G. & Goodenough, J. B. Structural and magnetic characterization of the lithiated iron oxide $Li_xFe_3O_4$. *J. Appl. Phys.* **59**, 1918–1926 (1986).
23. Zhang, W. et al. Insights into ionic transport and structural changes in magnetite during multiple-electron transfer reactions. *Adv. Energy Mater.* **6**, 1502471 (2016).
24. Permien, S. et al. What happens structurally and electronically during the Li conversion reaction of $CoFe_2O_4$ nanoparticles: an operando XAS and XRD investigation. *Chem. Mater.* **28**, 434–444 (2016).
25. Bock, D. C. et al. Size dependent behavior of Fe_3O_4 crystals during electrochemical (de)lithiation: an in situ X-ray diffraction, ex situ X-ray absorption spectroscopy, transmission electron microscopy and theoretical investigation. *Phys. Chem. Chem. Phys.* **19**, 20867–20880 (2017).
26. Komaba, S. et al. Electrochemical insertion of Li and Na ions into nanocrystalline Fe_3O_4 and α-Fe_2O_3 for rechargeable batteries. *J. Electrochem. Soc.* **157**, A60–A65 (2010).
27. Wang, F. et al. Conversion reaction mechanisms in lithium ion batteries: study of the binary metal fluoride electrodes. *J. Am. Chem. Soc.* **133**, 18828–18836 (2011).
28. Wang, J., Polleux, J., Lim, J. & Dunn, B. Pseudocapacitive contributions to electrochemical energy storage in TiO_2 (anatase) nanoparticles. *J. Phys. Chem. C* **111**, 14925–14931 (2007).
29. Augustyn, V. et al. High-rate electrochemical energy storage through Li^+ intercalation pseudocapacitance. *Nat. Mater.* **12**, 518–522 (2013).
30. Rondinelli, J. M., Stengel, M. & Spaldin, N. A. Carrier-mediated magnetoelectricity in complex oxide heterostructures. *Nat. Nanotechnol.* **3**, 46–50 (2008).
31. Maruyama, T. et al. Large voltage-induced magnetic anisotropy change in a few atomic layers of iron. *Nat. Nanotechnol.* **4**, 158–161 (2009).
32. O'Handley, R. C. *Modern Magnetic Materials: Principles and Applications* (Wiley, 2000).
33. Chen, C.-C., Fu, L. & Maier, J. Synergistic, ultrafast mass storage and removal in artificial mixed conductors. *Nature* **536**, 159–164 (2016).
34. Fu, L., Chen, C.-C., Samuelis, D. & Maier, J. Thermodynamics of lithium storage at abrupt junctions: modeling and experimental evidence. *Phys. Rev. Lett.* **112**, 208301 (2014).

35. Duan, C.-G. et al. Surface magnetoelectric effect in ferromagnetic metal films. *Phys. Rev. Lett.* **101**, 137201 (2008).
36. Hjortstam, O., Trygg, J., Wills, J. M., Johansson, B. & Eriksson, O. Calculated spin and orbital moments in the surfaces of the 3d metals Fe, Co, and Ni and their overlayers on Cu(001). *Phys. Rev. B* **53**, 9204–9213 (1996).
37. Coey, J. M. D. *Magnetism and Magnetic Materials* (Cambridge Univ. Press, 2010).

Publisher's note Springer Nature remains neutral with regard to jurisdictional claims in published maps and institutional affiliations.

© The Author(s), under exclusive licence to Springer Nature Limited 2020

Methods

Materials. Hollow Fe_3O_4 nanospheres were prepared by a hydrothermal method. A mixed aqueous solution (40 ml) that contained 2 mmol ferric chloride hexahydrate ($FeCl_3{\cdot}6H_2O$), 8 mmol sodium citrate dihydrate ($Na_3C_6H_5O_7{\cdot}2H_2O$), 6 mmol urea ($CH_4N_2O$) and 0.6 g sodium polyacrylate ($(C_3H_3NaO_2)_n$) was first prepared with vigorous stirring for 2 h. Then, the mixture was transferred to a 60 ml sealed Teflon-lined autoclave (Nanjing Zhengxin Instrument Co., Ltd.). The autoclave was placed in an oven and heated at 200 °C for 6 h, and then cooled to room temperature (28 °C). The precipitate was collected by centrifugation (8,000 r.p.m. for 5 min), washed repeatedly with distilled water and ethanol, and dried in an oven at 60 °C for 10 h. Finally, the product was annealed in argon at 500 °C for 2 h. An aberration-corrected JEM ARM200F STEM instrument (JEOL) provided a direct interpretation of the atomic structure.

Phase pure CoO and NiO were prepared by using the same hydrothermal method, by dissolving $Co(CH_3COO)_2{\cdot}4H_2O$ and $Ni(CH_3COO)_2{\cdot}4H_2O$ in ethylene glycol and heating in an oven at 200 °C for 4 h. After the products were washed and dried, they were annealed at 250 °C for 4 h in an argon atmosphere for CoO and at 300 °C for 4 h in air for NiO.

$(Fe(1\,nm)/TiO_2(3\,nm))_{15}$ and $(Fe(10\,nm)/TiO_2(3\,nm))_{15}$ films were prepared by layer-by-layer deposition with magnetron sputtering at a base pressure of 6×10^{-7} torr.

The Fe_2N was obtained by annealing the hollow Fe_3O_4 nanospheres in NH_3 at 900 °C for 3 h.

The FeF_2 was obtained by a solvothermal method. First, 0.71 g of ferric acetylacetonate and 1.2 g of polyvinylpyrrolidone were dissolved in 40 ml of isopropanol. Then, 3 ml of hydrofluoric acid were dropped into the solution, and the solution was stirred for 1 h. The mixture was transferred subsequently to a 60 ml sealed Teflon-lined autoclave and heated at 120 °C for 15 h. The precipitates were collected by centrifugation (8,000 r.p.m. for 2 min) and dried in vacuum for 12 h. Finally, the products were annealed at 300 °C for 6 h in an argon atmosphere.

Electrochemical testing. To prepare the Fe_3O_4 electrodes, the hollow Fe_3O_4 nanospheres were mixed with a conductive carbon black and polyvinylidene fluoride (PVDF) binder with an Fe_3O_4/conductive carbon black/PVDF weight ratio of 7:2:1 in an *N*-methyl-2-pyrrolidone solvent. The slurry was then coated onto copper foil and dried overnight at 110 °C under vacuum to remove the residual solvent. The CoO, NiO, FeF_2 and Fe_2N electrodes were prepared in a similar manner. The electrochemical properties were investigated in CR2032 coin-type cells by using 1 M $LiPF_6$ in 1:1 w/w ethylene carbonate/dimethyl carbonate as the electrolyte and lithium foil as the counter-electrode. Galvanostatic discharge–charge profiles were obtained by using a Landt CT2001A test system. Cyclic voltammetry and chronopotentiometry measurements were conducted with an electrochemical workstation (CHI660D, Chenhua Instruments) at a sweep rate of $0.25\,mV\,s^{-1}$.

In situ XRD. The evolution of phase and crystallinity of the Fe_3O_4 during the discharging–charging process were detected by using a specially designed in situ XRD electrochemical cell (assembled with a beryllium window as the current collector) that was positioned within a Rigaku Ultima IV diffractometer with Cu Kα radiation (λ = 1.5046 Å, 40 kV, 120 mA). XRD scans were collected continuously in a 2θ range of 10–80° at a scan rate of $15°\,min^{-1}$. A low-humidity dry room environment was ensured for all the measurements. The initial XRD scan of the Fe_3O_4 electrode was taken at the OCV; the electrode was then connected to the Landt CT2001A test system and lithiated or delithiated at a current density of $60\,mA\,g^{-1}$.

In situ magnetometry. The LIBs for the in situ magnetometry test were assembled by using a pouch-type cell in an argon-filled glovebox at room temperature. To prepare the cathode, the already-prepared Fe_3O_4/conductive carbon black/PVDF slurry with weight ratio of 7:2:1 was coated onto a rectangular copper current collector, and then dried at 80 °C under vacuum for 12 h before use. The CoO, NiO, FeF_2 and Fe_2N electrodes were prepared in a similar manner. The electrolyte solution was 1.0 M $LiPF_6$ in 1:1 w/w ethylene carbonate/dimethyl carbonate. A piece of lithium foil was used as the anode and a Celgard 2250 film (Whatman) was used as the separator. Polyethylene terephthalate sheets were used to seal the battery and make it flexible for in situ magnetization measurements. The magnetic properties were probed by a Quantum Design physical property measurement system magnetometer at 300 K. All in situ magnetization measurements were carried out simultaneously with the electrochemical discharge–charge processes in magnetic fields that were parallel to the copper foil.

Data availability

All data supporting the findings of this study are included in the paper and its Supplementary Information files. Source data are available from the corresponding authors upon reasonable request.

Acknowledgements

Q.L. and H.L. acknowledge support from the National Science Foundation of China (grant nos. 11504192, 51804173, 11434006 and 51673103), National Basic Research Program of China (no. 2015CB921502), National Key R&D Program of China (no. 2017YFA0303604), National Science Foundation of Shandong Province (no. ZR2018BB030), Science and Technology Program in Qingdao City (nos. 18-2-2-22-jch and 16-5-12-jch) and Youth Innovation Promotion Association of the Chinese Academy of Sciences (no. 2018008). G.Y. acknowledges financial support from a Welch Foundation award (no. F-1861), Sloan Research Fellowship and Camille Dreyfus Teacher-Scholar award. G.-X.M. acknowledges support from the Natural Sciences and Engineering Research Council of Canada (Discovery Grant no. RGPIN-04178) and Canada First Research Excellence Fund. J.S.M. acknowledges support from the National Science Foundation of the United States (grant no. DMR 1700137) and Office of Naval Research of the United States (grant no. N00014-16-1-2657).

Author contributions

Q.L., H.L., G.Y., G.-X.M. and J.S.M. conceived and designed the experiments. Q.X., Z.H., S.F. and X.S. carried out the synthesis and electrochemical tests. L.G. and Q.Z. performed STEM measurements. Q.L., H.L., X.W. and Q.X. carried out in situ magnetism measurements. G.-X.M., J.S.M., S.Y. and Y.L. assisted in the interpretation of the magnetization variation. H.L., Q.L., G.Y., Y.Z., C.G., G.-X.M. and J.S.M. analysed the data and co-wrote the paper. All authors discussed the experiments and final manuscript.

Competing interests

The authors declare no competing interests.

Additional information

Supplementary information is available for this paper at https://doi.org/10.1038/s41563-020-0756-y.

Correspondence and requests for materials should be addressed to Q.L., H.L., G.-X.M. or G.Y.

Reprints and permissions information is available at www.nature.com/reprints.